# Temperature effects on the aerodynamic and acoustic fields of a rectangular supersonic jet

Romain Gojon, Florian Baier, Ephraim J. Gutmark, Mihai Mihaescu

# Temperature effects on the aerodynamic and acoustic fields of a rectangular supersonic jet

Romain Gojon[1,*] , Florian Baier[2,†] , Ephraim Gutmark[2,‡] and Mihai Mihaescu[1,§]

*1. Department of Mechanics, Royal Institute of Technology (KTH)*

*Linné FLOW Centre*

*Stockholm, Sweden*

*2. Department of Aerospace Engineering & Mechanics*

*University of Cincinnati*

*Cincinnati, OH, United States*

**In the first part of the paper, a modified artificial dissipation mechanism permitting to perform Large-Eddy Simulations of highly compressible flows is proposed. This dissipation mechanism is evaluated using one linear 2-D test case and two non-linear 2-D test cases. In the second part, the flow and acoustic near-field of rectangular supersonic jets are explored using compressible LES based on this modified artificial dissipation mechanism. At the exit of a converging diverging rectangular nozzle of aspect ratio 2 and of design Mach number 1.5, the jets are overexpanded. Four simulations with four different temperature ratios ranging from 1 to 3 are performed in order to characterize the effect of the temperature on the aerodynamic and aeroacoustic fields of the jets. The geometry of the nozzle and the exit conditions are chosen in order to match those in the experimental study conducted at the University of Cincinnati. It is shown that the total number of cells in the shock cell structure decreases with the increase of the temperature ratio. However, the temperature does not influence the size of the first shock cell and the linear decrease of the shock cell size in the downstream direction. The Overall Sound Pressure Levels are then plotted along the minor and major axis. It is seen that the intensity of the screech feedback mechanism increases with the Temperature Ratio. Moreover, for JetTR25 and JetTR3, the strong flapping motion of the jet along the minor axis due to the screech feedback mechanism seems to yield to an asymmetric organization of the Mach wave radiation. The convection velocity of the turbulent structures in the jet shear layers along the minor axis is then studied. Once normalized by the jet exit velocity, the convection velocity is shown to decrease with the jet temperature ratio. In the last part of the paper, the near- and far-field acoustic are studied. In the near-field, screech tones which frequencies are consistent with both experimental data and a theoretical model are observed. In the far-field, four acoustic components typical of non-ideally supersonic jets are observed, namely the screech noise, the broadband shock-associated noise, the mixing noise and the Mach wave noise. Their directivities and frequencies are in agreement with experimental results and models.**

## I. Introduction

In future high-speed aircraft, rectangular propulsion systems closely integrated to the fuselage are considered. Supersonic non-ideally expanded jets exiting from such geometries can lead to very intense acoustic noise. Several acoustic components can be observed including screech noise, mixing noise, broadband shock-associated noise and Mach wave noise. The screech noise is due to an aeroacoustic feedback mechanism establishing between acoustic waves propagating upstream and turbulent structures propagating downstream.

*PostDoc, AIAA Member, gojon@kth.se

†PhD, AIAA Member, baierfn@mail.uc.edu

‡Distinguished Professor, Fellow AIAA, gutmarej@ucmail.uc.edu

§Associate Professor, Senior Member AIAA, mihai@mech.kth.se

This mechanism was described by Powell[1] and by Raman[2] and consists of two step. First, the turbulent structures developing in the jet shear layers and propagating in the downstream direction interact with the quasi-periodic shock cell structure of the jet, creating upstream propagating acoustic waves. Then, the resonant loop is closed at the nozzle trailing edge where the jet shear layers are excited when the upstream propagating acoustic waves impinge on the nozzle lips. Mixing noise is observed in both subsonic[3] and supersonic[4] jets. The directivity of this noise component is well marked around angles of 160 degrees with respect to the upstream direction and its dominant Strouhal number defined on the nozzle exit lengthscale and the jet ideally expanded velocity is around 0.2. This component is mainly generated at the end of the potential core[5–7]. For subsonic jets, Bogey and Bailly[5] proposed that this acoustic component is due to the intermittent intrusion of turbulent structures in the potential core. The broadband shock-associated noise (BBSAN) is produced by the interactions between the turbulent structures in the jet shear layers and the shock cell structure. In his pioneering work, Martlew[8] identified this noise. Several other experiments were conducted[9–11] and the central frequency of this noise component was found to vary with the angle in the far field. Harper-Bourne and Fisher[12] built a model which permits to predict the central frequency of this noise component as a function of the observation angle. Finally, the Mach wave radiation can be seen when the turbulent structures in the jet shear layers are convected at a supersonic speed. The Mach waves can simply be seen as shocks attached to a supersonic traveling object. Its directivity is given by the model of Oertel[13]. For the specific case of rectangular non-ideally expanded jets, a specific asymmetric shock pattern is observed[14] but the main acoustic sources are the same as the ones for round jets[4].

In the present paper, compressible jets exiting from a rectangular converging-diverging nozzle are simulated in order to study the influence of the temperature on the aerodynamic and acoustic fields of the jet. An experimental study of a similar jet is conducted at the University of Cincinnati[15]. The spectral and hydrodynamic properties of the jet are described and compared with experimental data and models. A modified artificial dissipation suitable for large-eddy simulations of highly compressible flows is proposed and assessed in section II. The jet parameters and the numerical methods used for the simulations are presented in section III. The aerodynamic and acoustic results are presented in section IV and V, respectively.

## II. The flow solver

### II.A. Numerical methods

The compressible flow solver[16] has already been used in previous studies by Semlitsch *et al.*[17,18] to perform Large Eddy Simulations of round non-ideally expanded supersonic jets. The simulations are carried out by using a finite volume method and by solving unsteady compressible Navier-Stokes equations on structured meshes. An explicit standard four-stage Runge-Kutta algorithm is used for time integration and a second order central difference scheme is used for spatial discretization. In order to improve the aeroacoustic capabilities of the solver, at the end of each time step, a modified artificial dissipation is added to the inviscid flows in order to remove grid-to-grid oscillations, to avoid Gibbs oscillations near shock and to relax subgrid-scale turbulent energy. This artificial dissipation has been designed on the same way as the one proposed by Jameson *et al.*[19] Moreover, in order to separate turbulent structures and shocks, a modification similar to the one proposed by Ducros *et al.*[20] has been used. Finally, the dissipation added to inviscid flows between the node 0 an the node 1 writes

$$D_{01} = \left[\epsilon_{01}^{(2)}(U_1 - U_0) - \epsilon_{01}^{(4)}(\Delta U_1 - \Delta U_0)\right]\phi_{01} r_{01} \tag{1}$$

where $U_0$ is the value of the inviscid flow considered at the node 0, $\epsilon_{01}^{(2)}$ and $\epsilon_{01}^{(4)}$ are the dissipation functions, $\Delta$ is the Laplacian operator, $\phi_{01}$ is the spectral radius and $r_{01}$ is a function depending on the grid stretching.

The dissipation functions write

$$\begin{cases} \epsilon_{01}^{(2)} = max(\epsilon_0^{(2)}, \epsilon_1^{(2)}) \\ \epsilon_{01}^{(4)} = (1/2 + 1/2 min(max(\Phi_0, \Phi_1), max(\Theta_0, \Theta_1)))max(0, C_4 - \epsilon_{01}^{(2)})s_4 \end{cases} \tag{2}$$

with

$$\epsilon_0^{(2)} = C_2 \Phi_0 \left(\frac{|\sum p_k - p_0|}{\sum p_k + p_0}\right) s_2,\ \Phi_0 = \frac{(\nabla . u_0)^2}{(\nabla . u_0)^2 + \omega^2} \text{ and } \Theta_0 = \frac{\omega^2}{(\nabla . u_0)^2 + \omega^2}$$

where $u_0$ is the velocity at the node 0, $\omega$ is the vorticity, $C_2$ and $C_4$ are constants to define, $p_0$ is the pressure in the node 0 and $s_2$ and $s_4 = s_2^2/4$ are scaling factors which permit to take into account the number of neighbors. $\Phi_0$ varies between 0 for weakly compressible regions to about 1 in shock regions. The capabilities of this dissipation mechanism were assessed for three aeroacoustic test cases, namely an acoustic pulse, a shock propagation and a shock-vortex interaction. Based on this validation, the constants values were set to $(C_2, C_4) = (1.5, 0.04)$. The results for those values are given in the following section.

## II.B. 2-D test cases

For the three considered test cases, the variables are nondimensionalized. The first test case is a linear problem and the two others correspond to non-linear problems in order to assess the aeroacoustic capabilities of the solver in highly compressible flows.

### *II.B.1. Acoustic pulse*

The first test case proposed is a Gaussian acoustic pulse placed in a uniform flow. This 2-D test case have been proposed in the first ICASE/LaRC Workshop[21]. The mean density and the mean pressure are equal to $\overline{\rho} = 1$ and $\overline{p} = 1/\gamma$ where $\gamma = 1.4$ is the heat capacity ratio. The mean velocity field is equal to $(u, v) = (M, 0)$ where $M = 0.5$. The initial perturbation, consisting of a Gaussian acoustic pulse centered at $(x, y) = (0, 0)$, can be written

$$\begin{cases} p'(x,y) = \epsilon \exp(-ln(2)/b^2(x^2+y^2)) \\ \rho'(x,y) = \epsilon \exp(-ln(2)/b^2(x^2+y^2)) \\ u'(x,y) = 0 \\ v'(x,y) = 0 \end{cases} \tag{3}$$

where $\epsilon = 0.001$ is the amplitude of the pulse and $b = 3$ is the Gaussian half-width.

This problem is solved on a uniform grid with $\Delta x = \Delta y = 0.2$ with a temporal discretization of $\Delta t = 2/30$ in order to have a Courant number $CFL = (u + c)\Delta t/\Delta x = 0.5$. The results at three time intervals are represented in Figure 1.

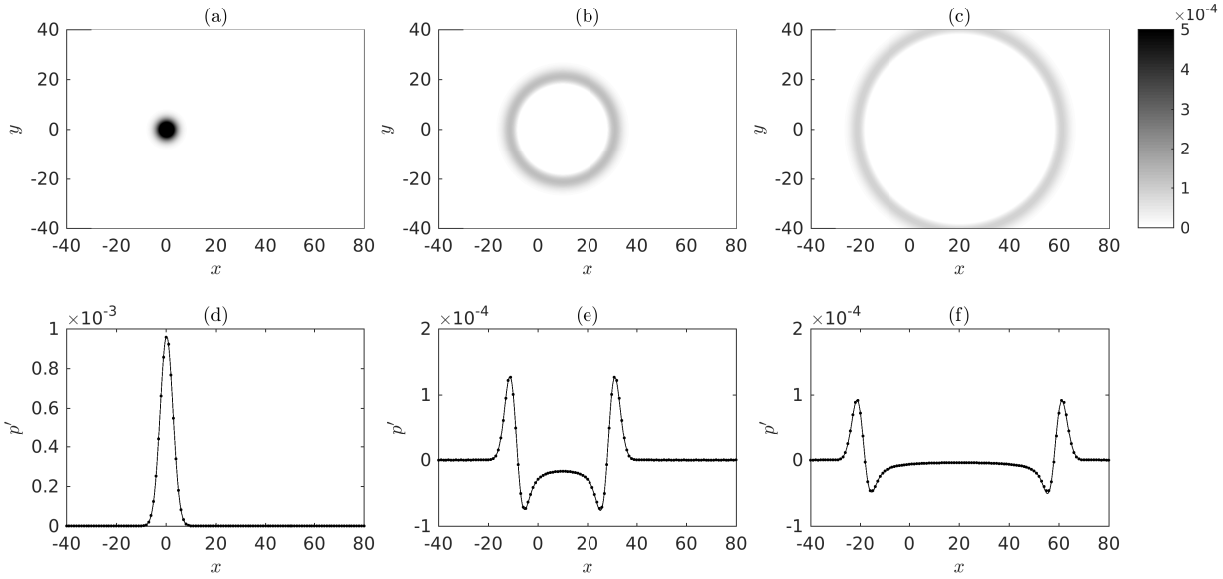


**Figure 1. (a,b,c) Snapshots of the fluctuating pressure field and (d,e,f) cut along the line $y = 0$ at times (a,d) $t = 0.5$, (b,e) $t = 20$ and (c,f) $t = 40$; • analytical solution and —— present simulation.**

For this canonical linear flow scenario, an analytical solution can be found from the linearized Euler equations. The 2-D solution can be found in Tam and Webb[22] and the 3-D solution can be found in Bogey and Bailly[23]. In 2-D, the analytical solution writes

$$p'(x,y,z) = \rho'(x,y,t) = \frac{\epsilon}{2\alpha}\int_0^\infty \exp(-\xi^2/4\alpha)\cos(\xi t)J_0(\xi\eta)\xi d\xi \tag{4}$$

where $\alpha = ln(2)/b^2$, $\eta = \left[(x-Mt)^2+y^2\right]^{1/2}$ and $J_0$ is the Bessel function of the first kind and of order 0.

The analytical solution has been added in Figure 1 for the three time instances considered. A perfect match is visible between the analytical solution and the simulation results.

### *II.B.2. Shock propagation*

The second 2-D test case is a non-linear propagation of a shock. This problem is also proposed in the first ICASE/LaRC Workshop[21]. The mean density and the mean pressure are equal to $\overline{\rho} = 1$ and $\overline{p} = 1/\gamma$. The mean velocity field is equal to $(u,v) = (0,0)$. The initial field is given by

$$\begin{cases} u(x,y) = 0.5\exp\left(-ln(2)(x/5)^2\right) \\ v(x,y) = 0 \\ p(x,y) = 1/\gamma\left(1+\dfrac{\gamma-1}{2}u\right)^{\dfrac{2\gamma}{\gamma-1}} \\ \rho(x,y) = \left(1+\dfrac{\gamma-1}{2}u\right)^{\dfrac{2}{\gamma-1}} \end{cases} \tag{5}$$

An uniform grid with $\Delta x = \Delta y = 1$ is used to solve this problem. A temporal discretization of $\Delta t = 1/3$ is chosen, yielding a Courant number $CFL = (u+c)\Delta t/\Delta x = 0.5$. The results along the line $y = 0$ at three time instances are represented in Figure 2. The numerical results from Bogey *et al.*[24] are added for comparison. A very good match is found with the position, the amplitude and the shape being in agreement. An oscillatory behavior can however be seen in the present simulation.

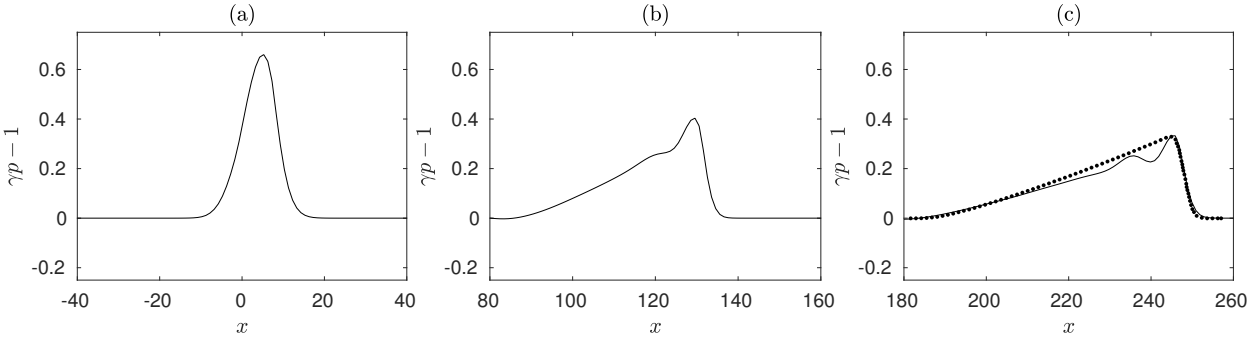


**Figure 2. (a,b,c) cut along the line $y = 0$ of the fluctuating pressure $\gamma p - 1$ at times (a) $t = 0.6$, (b) $t = 100$ and (c) $t = 200$; • solution found by Bogey and Bailly[24] and —— present simulation.**

### *II.B.3. Shock-vortex interaction*

The third 2-D test case is the non-linear interaction between a vortex and a shock. The mean field is a normal shock at $x = 0$ characterized by an upstream Mach number $\mathcal{M}_1 = u_1/c_0 = 1.2$. The mean flow upstream and downstream from the shock are given by

$$\begin{cases} u_1 = 1.2 \\ v_1 = 0 \\ \rho_1 = 1 \\ p_1 = 1/\gamma \end{cases} \qquad \begin{cases} u_2 = u_1\dfrac{(\gamma-1)\mathcal{M}_1^2+2}{(\gamma+1)\mathcal{M}_1^2} \\ v_2 = 0 \\ \rho_2 = \rho_1\dfrac{u_1}{u_2} \\ p_2 = p_1\dfrac{\dfrac{\rho_2}{\rho_1}(\gamma+1)-(\gamma-1)}{(\gamma+1)-\dfrac{\rho_2}{\rho_1}(\gamma-1)} \end{cases} \tag{6}$$

where the subscripts 1 and 2 denote the upstream and downstream parts of the normal shock.

The initial perturbation, consisting of a single vortex centered at $(x, y) = (-2, 0)$, is characterized by the velocity distributions of a Taylor vortex. Its velocity components in the cylindrical coordinate system centered at $(x, y) = (-2, 0)$ can be written

$$\begin{cases} u_r(r)' = 0 \\ u_\theta(r)' = \mathcal{M}_v r \exp \dfrac{1 - r^2}{2} \end{cases} \tag{7}$$

The density and pressure in the vortex region can then be written

$$\begin{cases} \rho(r) = \left(1 + \dfrac{\gamma - 1}{2} \mathcal{M}_v^2 \exp(1 - r^2)\right)^{\dfrac{1}{\gamma - 1}} \\ p(r) = \dfrac{1}{\gamma} \rho(r)^\gamma \end{cases} \tag{8}$$

where $\mathcal{M}_v = 0.25$.

The simulation has been performed on a uniform grid with a mesh spacing equal to $\Delta x = \Delta y = 0.2$ with a temporal discretization of $\Delta = 0.05$, yielding $CFL = (u_1 + c)\Delta t / \Delta x = 0.55$. Snapshots of the pressure field are represented in Figure 3 for four different times. In Figure 3(a), at $t = 0$, the Taylor vortex is located just upstream from the normal shock, at $(x, y) = (-2, 0)$. The vortex then passes through the normal shock, creating an acoustic wave in the process, visible in Figure 3(b,c,d), at $t = 10$, $t = 20$ and $t = 30$.

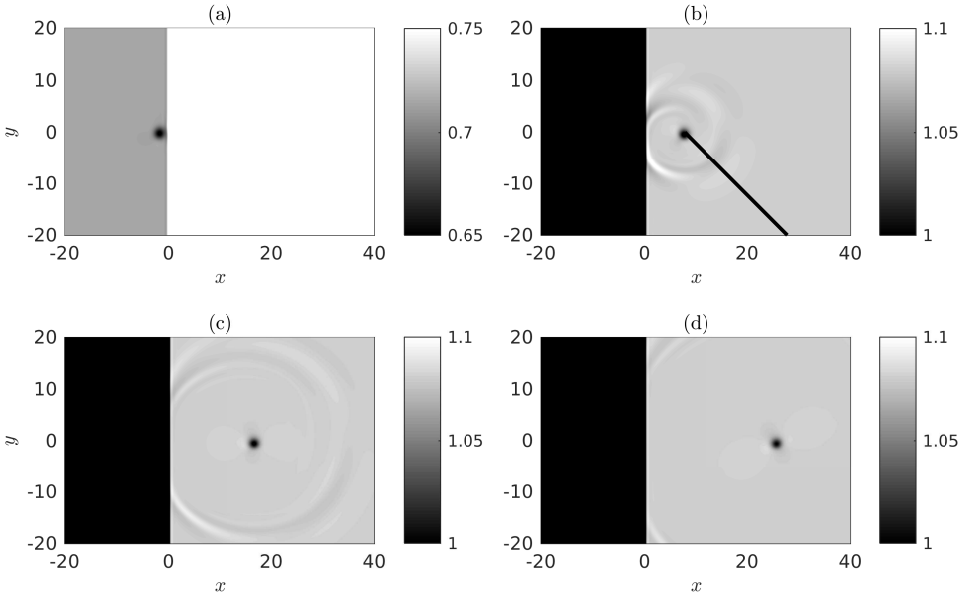


**Figure 3. Snapshots of the pressure field at times (a) $t = 0$, (b) $t = 10$, (c) $t = 20$ and (d) $t = 30$.**

The results are then compared to the Direct Numerical Simulation results obtained by Inoue[25] along the line starting from the center of the vortex and making an angle of $-45$ degrees compared to the downstream direction. The line is represented in Figure 3(b) for clarity. The comparison is proposed in Figure 4. An excellent agreement is visible. The acoustic wave created by the interaction between the shock and he vortex has the same amplitude, the same propagation speed and the same shape as the one in the Direct Numerical Simulation.

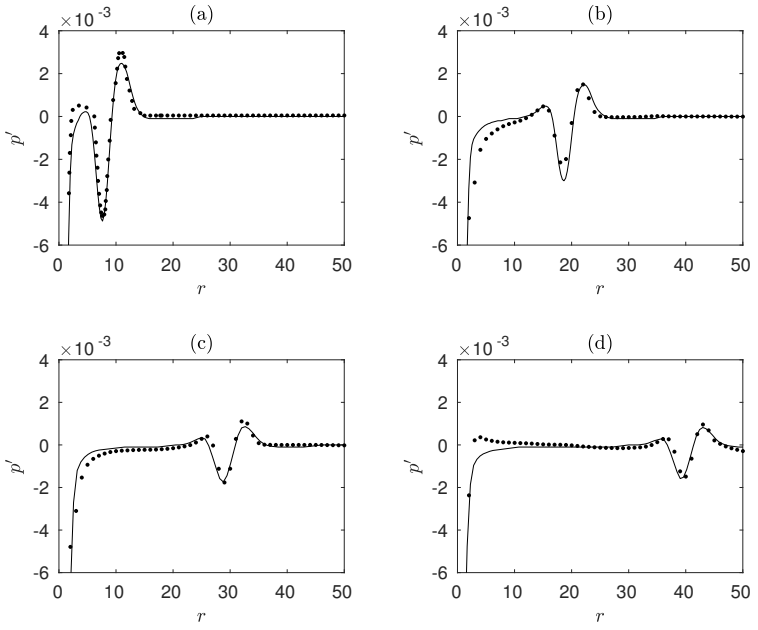


**Figure 4. Radial distribution of the fluctuating pressure starting from the center of the vortex along the line making an angle of −45 degrees compared to the downstream direction at (a) $t = 10$, (b) $t = 20$, (c) $t = 30$ and (d) $t = 40$; • Direct Numerical Simulation results obtained by Inoue[25] and —— present simulation.**

# III. The rectangular supersonic jet

## III.A. Jet parameters

Four Large Eddy Simulations of supersonic rectangular jets are performed, corresponding to four Temperature Ratios (TR) of 1, 2, 2.5 and 3. The jets will be referred as JetTR1, JetTR2, JetTR25 and JetTR3 respectively. The different cases are presented in Table 1. The jets originate from a rectangular converging-diverging nozzle of aspect ratio (AR) of $2:1$, which has a height of $h = 12.95$mm in the minor axis plane. The design Nozzle Pressure Ratio of this nozzle is 3.67, yielding a Mach design of $\mathcal{M}_d = 1.5$. In this study, the jets are overexpanded with a Nozzle Pressure Ratio (NPR) of 3. The geometry and the operating conditions are similar to those in the experimental study of Mora *et al.*[15]

| | $NPR$ | $\mathcal{M}_j$ | $TR$ | $u_j$ (m.s$^{-1}$) |
|---|---|---|---|---|
| JetTR1 | 3 | 1.36 | 1. | 398 |
| JetTR2 | 3 | 1.36 | 2. | 563 |
| JetTR25 | 3 | 1.36 | 2.5 | 629 |
| JetTR3 | 3 | 1.36 | 3 | 689 |

**Table 1. Jet parameters: Nozzle Pressure Ratio $NPR$, ideally expanded Mach number $\mathcal{M}_j$, Temperature Ratio $TR$ and ideally-expanded jet velocity $u_j$.**

## III.B. Convergence study

The Large Eddy Simulations are carried out using the compressible flow solver[16] with the modifications presented in section II.A. First, a convergence study have been carried out for the cold jet JetTR1. Three structured meshes consisting of 64 blocks were designed with 40, 80 and 160 millions of nodes respectively. A visualization of the converging diverging nozzle along the minor axis plane is proposed in Figure 5(a) picturing half the nozzle[15]. In Figure 5(b), the intermediate structured mesh along the same plane is represented. It can be noted that the finest mesh has been designed in order to have a mesh size of $y^+ \sim 1$ in the wall normal direction and of $x^+ < 10$ in the wall parallel directions in the diverging part of the nozzle. Moreover, the stretching of the mesh is kept below 5% in the domain of interest to preserve numerical accuracy.

Total temperature and total pressure are imposed at the inlet of the nozzle. Characteristic boundary

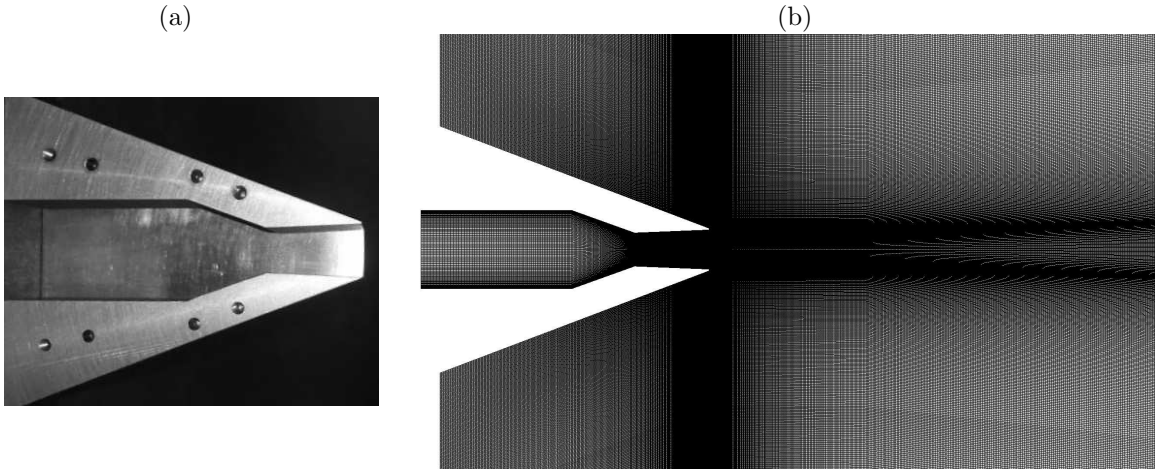


**Figure 5. (a) Picture of half the nozzle showing the converging diverging geometry along the minor axis and (b) 80 millions of nodes structured mesh along the same plane.**

conditions are applied on all the other boundaries. Those conditions combined with the implementation of sponge zones permit avoiding spurious reflections in the physical domain. Finally, adiabatic no-slip conditions are used at the nozzle walls. Visulatizations of the flow and near-field acoustics as calculated with two different grid resolutions, namely 40 and 160 millions of nodes are represented in Figure 6. The pressure fields along the major axis are also shown. Qualitatively, when the number of nodes increases, smaller structures are observed in the jet shear-layers and higher frequencies are propagated in the surrounding near acoustic field.

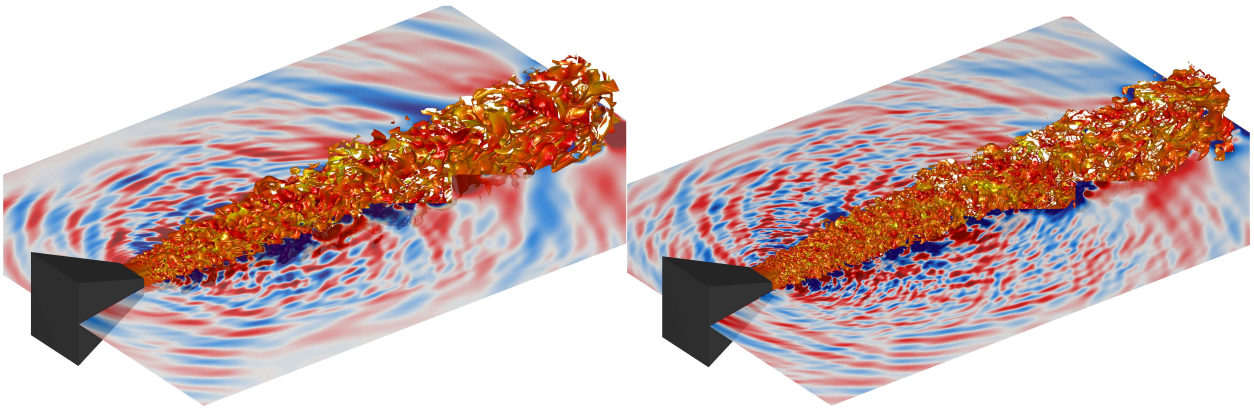

**Figure 6. Isosurfaces of density for the cold jet JetTR1 with a (left) 40M nodes and (right) 160M nodes meshes. The isosurfaces for 1.2 kg.m$^{-3}$ are represented colored by the Mach number. The pressure field along the major axis is also shown. The nozzle is in black.**

Data obtained with LES for the three different grid resolutions are compared in Figure 7 with experimental results along the jet axis and along the minor/major axis on the plane $z = 2h$. The shock-cell structure and the levels obtained in the LES and in the experiment are overall in good agreement. However, when increasing the number of nodes, the length of the shock cells follows better the experimental results. The mesh with 160 millions of nodes will be used in this study, as it permits to follow better the shock cell structure observed experimentally and to propagate higher frequencies in the near acoustic field. Please note that the 160 millions of nodes mesh has been designed in order to allow acoustic waves with Strouhal numbers up to $St = fD_{eq}/u_j = 3$ to be well propagated, where $f$ is the frequency, $D_{eq}$ is the equivalent diameter of the jet, and $u_j$ is the ideally expanded jet velocity.

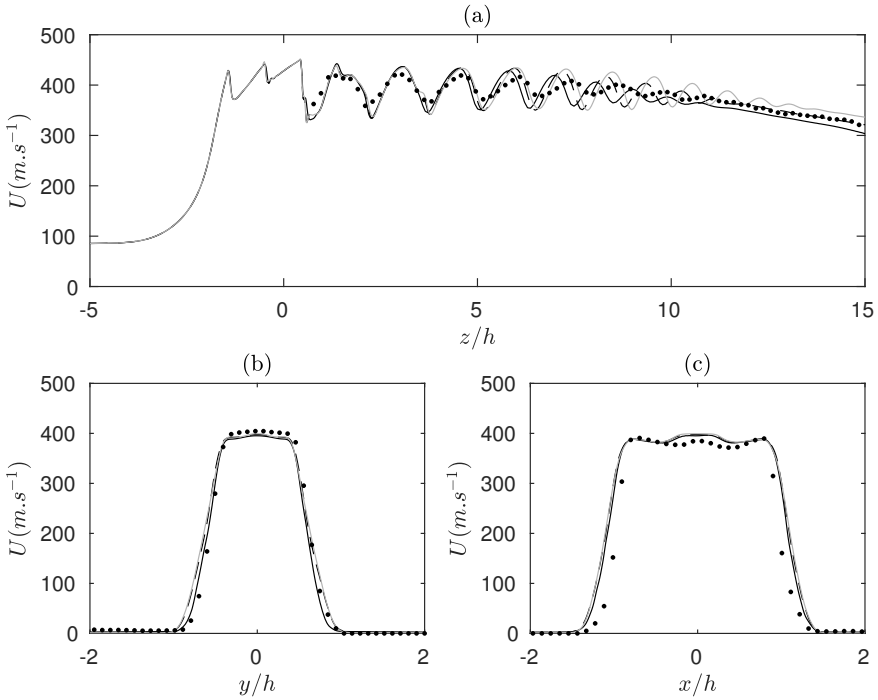


**Figure 7. Mean axial velocity field for the cold jet JetTR1 along (a) the jet axis, (b) the minor axis at $z = 2h$ and (c) the major axis at $z = 2h$; • PIV results and —— 40M, — — — 80M and —— 160M LES results.**

# IV. Aerodynamics results

The four LES simulations (see Table 1) are performed on the 160 millions of nodes mesh. A total of $200,000$ time steps of $\Delta t = 0.002h/u_j$ are computed in each case after the transient period, permitting a simulation time of $400h/u_j$.

## IV.A. Instantaneous features

In order to visualize simultaneously the jet flow and the near acoustic field, three-dimensional snapshots are displayed in Figure 8 for JetTR1, JetTR2 and JetTR3. The jet shear-layers are shown using isosurfaces of density and the near acoustic fields of the jets along the minor axis and along the major axis are represented using the instantaneous pressure.

In Figure 8(a,b), for the cold jet ($TR = 1$), three features are observed in the near acoustic field. First, acoustic waves propagating in the upstream direction in the vicinity of the nozzle are visible. These waves are linked to the screech noise. This noise component have been observed in various studies, notably in Westley and Woolley[26], Tam and Tanna[9], Panda *et al.*[27], and André *et al.*[28] The second acoustic contribution that can be seen consists of circular acoustic waves coming from the jet shear layers at different axial positions. These acoustic waves are due to the interactions between the turbulent structures and the shock cell structure in the jet shear-layers. Those interactions lead to the observation of broadband shock-associated noise in the far-field[9,11,29]. The third acoustic component visible propagates in the downstream direction and is associated to a low frequency. This acoustic contribution corresponds to the mixing noise, as observed by Bogey and Bailly[5], Sandham and Salgado[6] and Tam[7] for instance.

In Figure 8(c-f), for the higher temperature ratios investigated ($TR = 2$ and $TR = 3$) it can be observed a temperature effect on the amplitude of the upstream propagating waves. One have to note that the amplitude of the upstream propagating waves is stronger along the minor axis plane than along the major axis one. Moreover, these waves are visibly antisymmetrically organised with respect to the jet axis. These two observations suggest that the screech mechanism in those jets is associated with a flapping motion of the jets along the minor axis. Moreover, it seems that the amplitude of the screech noise is increasing with the temperature. Secondly, when the Temperature Ratio increases, a new acoustic component arises in the sideline direction with long and straight acoustic waves organized along a clear direction. This acoustic

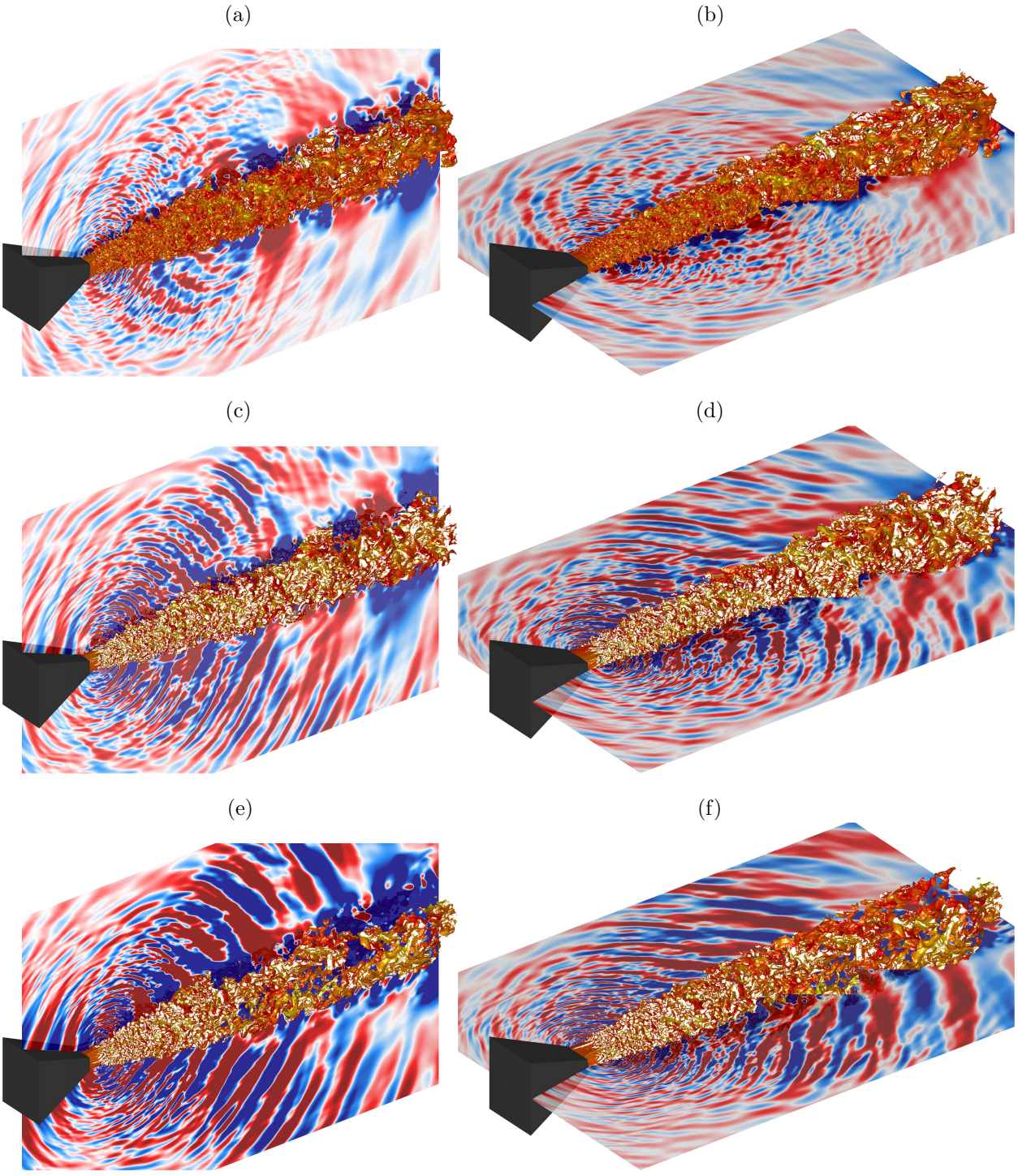


**Figure 8.** Isosurfaces of density colored by the Mach number for (a,b) JetTR1, (c,d) JetTR2 and (e,f) JetTR3. The pressure field along (a,c,e) the minor axis and (b,d,f) the major axis are also shown. The nozzle is in black.

contribution is linked to Mach wave radiation. This specific noise component appears when the convection velocity of the turbulent structures in the jet shear-layers becomes supersonic. This acoustic component have a marked directivity and a broadband spectrum. It has been studied experimentally [30] and numerically [31].

### IV.B. Flow field statistics

The mean axial velocity fields obtained in the present LES for the four Temperature Ratios are represented in Figure 9. For JetTR1, JetTR2 and JetTR3, they are compared to experimental PIV results in Figure 9(a,b,c,e). Despite of the unavoidabale mismatch in the boundary conditions between the simulations and experiments there is an overall good agreement between the two sets of data. Moreover, as noted by Hsia *et al.* [32] for subsonic jets and by Zaman [33] for supersonic jets, a turbulent rectangular jet spreads faster along its minor axis than along its major axis, evolving from a rectangular cross section to a circular cross section. This evolution is clearly visible in Figure 9 where the jets appear circular at $z = 15h$.

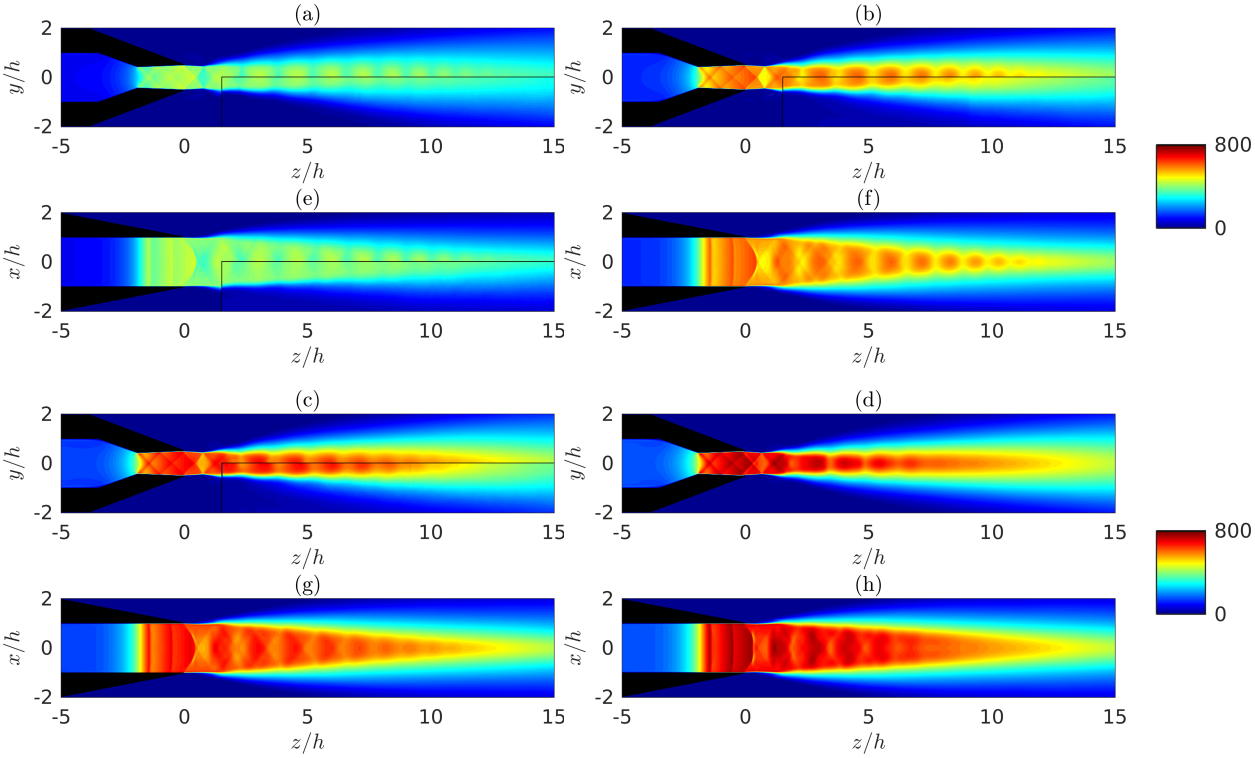


**Figure 9. Mean axial velocity field for (a,e) JetTR1, (b,f) JetTR2, (c,g) JetTR25 and (d,h) JetTR3 along (a,b,c,d) the minor axis and (e,f,g,h) the major axis. The PIV results are added in the black rectangles. The nozzle is in black.**

In Figure 9, it can be observed that the length of the shock cells decreases in the downstream direction. This trend is due to the growth of the shear layer and to the dissipation of the shock-cell structure by the turbulence [34]. For rectangular jets, Tam [35] built a model by considering the corresponding rectangular ideally expanded jet to predict the length of the first shock cell. The model gives

$$L_{model} = 2(\mathcal{M}_j^2 - 1)^{1/2} \frac{h_j}{(1 + h_j^2/b_j^2)^{1/2}} \tag{9}$$

where $h_j$ and $b_j$ are the dimensions of the corresponding ideally expanded rectangular jet. For our aspect ratio 2 rectangular nozzle, their expressions [35] can be reduced to

$$\frac{h_j}{h} = [(A_j/A_d) - 1] * 2/3 + 1$$

$$\frac{b_j}{2h} = [(A_j/A_d) - 1] * 1/3 + 1$$

where $A_j$ is the nozzle exit area of the fully expanded equivalent jet and $A_d = h * 2h$ is the nozzle exit area. $A_j$ is given by

$$\left(\frac{A_j}{A_d}\right)^2 = \frac{\mathcal{M}_d^2}{\mathcal{M}_j^2}\left[(1+\frac{\gamma-1}{2}\mathcal{M}_j^2)/(1+\frac{\gamma-1}{2}\mathcal{M}_d^2)\right]^{(\gamma+1)/(\gamma-1)}$$

where $\mathcal{M}_d = 1.5$ is the design Mach number of the nozzle.

Equation (9) permits to find a value $L_{model} = 1.57h$. Values of $L_s = 0.99L_{model}$, $L_s = 0.97L_{model}$, $L_s = 0.97L_{model}$ and $L_s = 0.95L_{model}$ are found for the size of the first shock cell of JetTR1, JetTR2, JetTR25 and JetTR3, respectively. The size of the cell decreases by few percent with the jet temperature ratio but overall, the model gives a very good approximation for the length of the first shock cell. The normalized shock cell size $L_s/L_{model}$ are reported in Figure 10 for all the visible cells in the mean fields of all investigated temperature ratios. The total number of shock cells visible decreases with the temperature ratio, from 10 for $TR = 1$ to 4 for $TR = 3$. However, the variation of the shock-cell size appears to behave linearly for the four jets. Such evolution was already observed by Harper-Bourne and Fisher[12] for round supersonic jets. They proposed a relation for the size of the $n$-th shock cell which writes

$$L_n = L_s - (n-1)\Delta L \tag{10}$$

where $\Delta L$ is the variation of the cell size from one cell to another. For the present jets, a mean value of $\Delta L/L_s = 5.5\%$ is obtained. For round underexpanded supersonic jets, André *et al.*[28] and Harper-Bourne and Fisher[12] found $\Delta L/L_s = 3\%$ and $\Delta L/L_s = 6\%$, respectively. It is worth noting that the lower value found by André *et al.*[28] can be attributed to the presence of a secondary flow characterized by a Mach number of 0.05. To conclude, for our rectangular aspect ratio 2 jet, a linear evolution of the shock cell size similar to the one in round jets is observed.

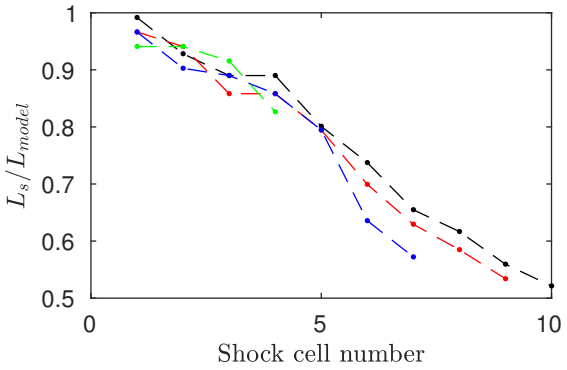


**Figure 10. Normalized lengths of the shock cells obtained for – • – JetTR1, – • – JetTR2, – • – JetTR25, and – • – JetLTR3.**

Overall Sound Pressure Levels (OASPL) obtained along the minor and the major axis are represented for the four jets in Figure 11. Isocontours are added in order to improve the readability. The OASPL is computed from the rms pressure fields. Several acoustic components are visible. The first acoustic component is visible in Figure 11(a,b,c,d) in the upstream direction along the minor axis plane. This component is linked to acoustic waves propagating in the upstream direction, permitting to close the aeroacoustic feedback loop leading to the screech noise. This acoustic component is only visible along the minor axis and its amplitude increases with the Temperature Ratio, confirming the observations made in Figure 8. Moreover, the cell structures obtained in the jets shear-layers in the amplitude fields of figure 11(c,d) for Temperatures Ratio of 2.5 and 3 are due to the presence of hydrodynamic-acoustic standing waves creating by the screech feedback loop, explaining their presence only along the minor axis plane. Such structures were previously observed by Panda *et al.*[27] for screeching supersonic jets and by Gojon *et al.*[36] for ideally expanded planar impinging jets. The second acoustic components visible is linked to the Mach wave noise, whose intensity increases with the Temperature Ratio. Moreover, it can be seen that this component is organized in a axisymmetric manner for JetTR2 in Figure 11(b,f) but in a asymmetric manner for JetTR25 and JetTR3 in Figure 11(c,d,g,h) with a lot stronger Mach wave radiation along the minor axis compared to the major axis. The strong flapping motion of the jet along the minor axis due to the screech feedback mechanism seems to lead to this asymmetric organization of the Mach wave radiation.

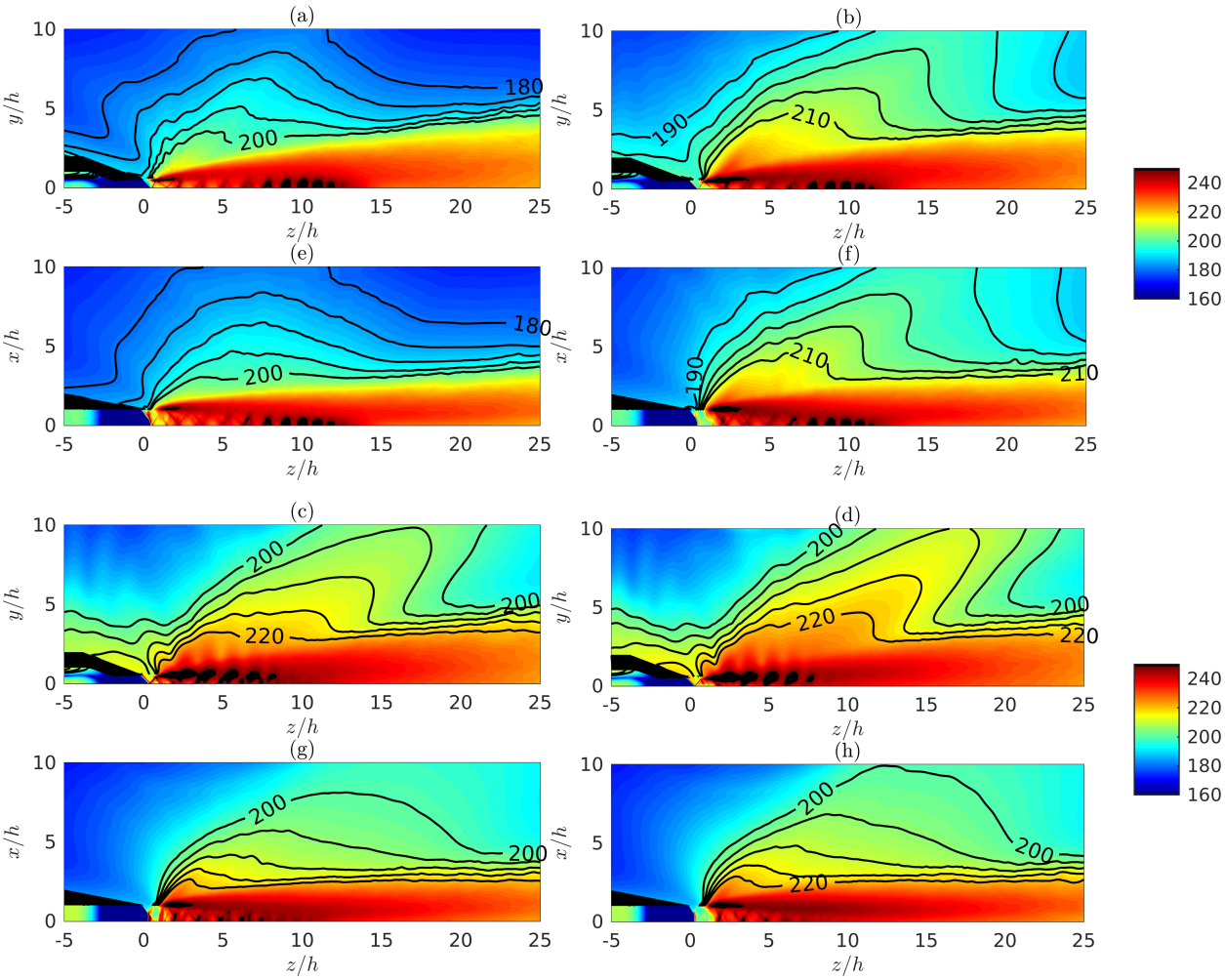


**Figure 11. Overall Sound Pressure Levels for (a,e) JetTR1, (b,f) JetTR2 (c,g) JetTR25 and (d,h) JetTR3 along (a,b,c,d) the minor axis and (e,f,g,h) the major axis. The nozzle is in black.**

### IV.C. Temperature effect on convection velocity

In order to assess the presence of the Mach wave radiation in the hot cases, the convection velocity of turbulent structures in the jet shear layers is computed. It is calculated in the jet shear layers, where the turbulence kinetic energy is maximum, from cross-correlations of axial velocity between 70 neighbors points equidistantly spaced at $0.25h$ from each other. For the four jets, the normalized convection velocity and the convective Mach number along the jet shear layer in the minor axis are represented in Figure 12. For all the jets, the convection velocity is not constant but varies according to the shock cell structure, as already observed for round jets experimentally[10] and numerically[37]. The mean values of the convection velocity and of the convective Mach number between $z = 1$ and $z = 15$ along the minor axis are reported in Table 2. Overall, the mean normalized convection velocity $< u_c >$ of the turbulent structures decreases with the increase of the Temperature Ratio, from $0.80u_j$ to $0.64u_j$. The same observation has been made numerically in a recent study by Liu *et al.*[38] Indeed, for round supersonic underexpanded jets, they found a convection velocity decreasing from $0.68u_j$ for a Temperature Ratio of 1 to $0.56u_j$ for a Temperature Ratio of 7. In Figure 12(b), the convective Mach number remains below 1 for JetTR1, yielding the absence of Mach waves in Figure 8(a,b). For JetTR2, JetTR25 and JetTR3, a convective Mach number of about $\mathcal{M}_c = 1.25$ is found. This supersonic Mach number yields the creation of the Mach waves observed in Figure 8(c-f).

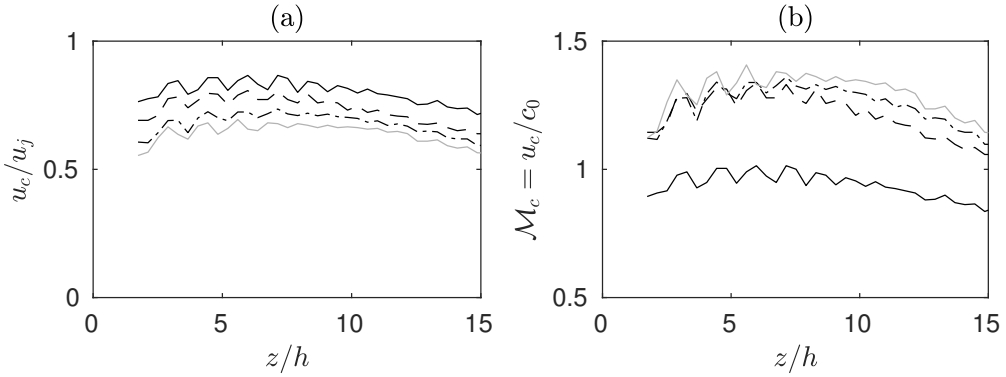


**Figure 12. (a) Convection velocity and (b) convective Mach number $\mathcal{M}_c$ of the turbulent structures along the jet shear-layer in the minor axis plane as functions of the axial position for —— JetTR1, — — — JetTR2, —·— JetTR25, and —— JetLTR3.**

| | $u_j$ (m.s$^{-1}$) | $< u_c/u_j >$ | $\mathcal{M}_c =< u_c/c_0 >$ |
|---|---|---|---|
| JetTR1 | 398 | 0.80 | 0.94 |
| JetTR2 | 563 | 0.73 | 1.21 |
| JetTR25 | 629 | 0.68 | 1.25 |
| JetTR3 | 689 | 0.64 | 1.29 |

**Table 2. Convection velocity along the minor axis: ideally expanded velocity $u_j$, mean convection velocity $< u_c/u_j >$ and mean convective Mach number $\mathcal{M}_c =< u_c/c_0 >$.**

## V. Acoustic results

### V.A. Near-field acoustics

The pressure spectra obtained in the vicinity of the nozzle at $(x, y, z) = (0, -2h, -2h)$ are represented in Figure 13 as functions of the Strouhal number $St = fD_{eq}/u_j$. There is a change in the dominant frequency as the jet's temperature is changing, with dimensionless frequencies ranging between $St = 0.29$ and $St = 0.36$. Those frequencies, visible in the upstream direction in the vicinity of the jet, correspond to screech components, see for instance in Westley and Woolley[26], Tam and Tanna[9], Panda *et al.*[27], and André *et al.*[28] Two other secondary tones can be seen in the spectra in Figure 13; a low frequency ranging between $St = 0.16$ and $St = 0.21$ and the first harmonic of the screech frequency.

For the four jets, the amplitude and the frequency of the low frequency and screech components are given in Table 3. The screech frequencies found experimentally[15] are also reported. For the low frequency

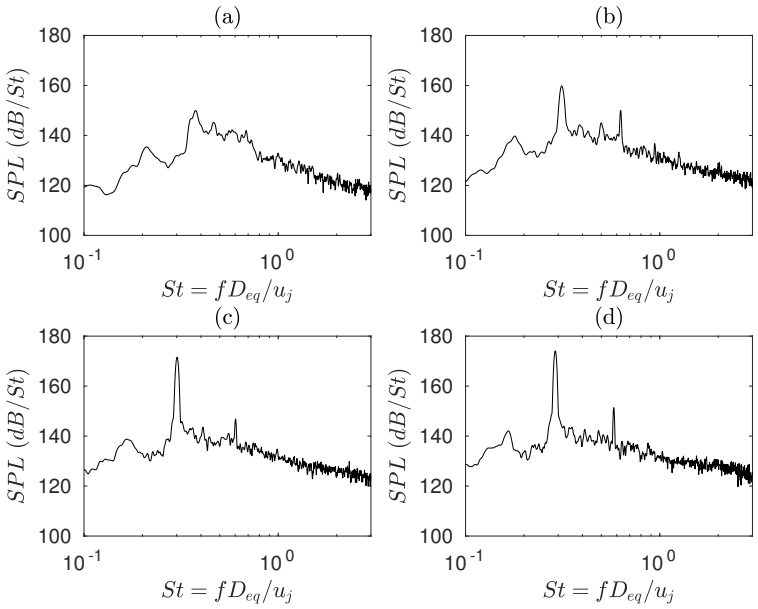


**Figure 13. Pressure spectra at $(x, y, z) = (0, -2h, -2h)$ as functions of the Strouhal number for (a) JetTR1, (b) JetTR2, (c) JetTR25 and (d) JetTR3.**

component, its Strouhal number is decreasing with the temperature ratio from $St = 0.21$ for JetTR1 to $St = 0.16$ for JetTR3, with an amplitude globally increasing from 135dB/St for JetTR1 to 142dB/St for JetTR3. For the screech component, the Strouhal number is decreasing from $St = 0.36$ for JetTR1 to $St = 0.29$ for JetTR3 and the amplitude is increasing from 150dB/St for JetTR1 to 174dB/St for JetTR3. The Strouhal numbers are in excellent agreement with the experimental results from the University of Cincinnati[15]. Please note that those frequencies have been reported using a far-field microphone array organized along the minor axis. However, Mora *et al.*[15] observed an overall decrease of the amplitude of the screech component with an increase of the Temperature Ratio, in contradiction with the present increase observed. It is believed that this behavior is due to the lack of turbulence at the nozzle exit in the simulations. For a rectangular jet, Tam[35] built a model in order to predict the screech frequency. In the present scenario (2:1 AR rectangular jet), the model writes

$$St_{Tam} = \frac{\dfrac{D_{eq}u_c/u_j}{2h(1+u_c/a_0)(\mathcal{M}_j^2-1)^{1/2}}\left((h_j/b_j)^2+1\right)}{\left(\left(\dfrac{1+\dfrac{\gamma-1}{2}\mathcal{M}_j^2}{1+\dfrac{\gamma-1}{2}\mathcal{M}_d^2}\right)^{(\gamma+1)/(2(\gamma-1))}\dfrac{\mathcal{M}_d}{\mathcal{M}_j}-1\right)\dfrac{2}{3}+1} \tag{11}$$

The values found by evaluating equation (11) using the mean convection velocity and mean convective Mach number from Table 2 are reported in Table 3. For JetTR2, JetTR25, and JetTR3, a very good agreement is found between the simulation results, the experimental results, and the value found using equation (11). For JetTR1, equation (11) yields to an overestimation of about 10% of the screech frequency. Overall, the decrease of the frequency of the screech component with the Temperature Ratio is recovered using equation (11).

### V.B. Far-field acoustics

The Ffowcs Williams-Hawkings (FW-H) surface used to compute the far-field acoustics is an ellipsoid represented in Figure 14 along the minor axis for the case JetTR2. It is placed at the end of the first acoustic zone in the structured mesh, corresponding to a Strouhal number resolved of $St \sim 6$. The surface consists of about 1 million nodes and the flow variables are stored at a sampling frequency corresponding to $St \sim 10$. Please note that the surface is placed comparatively to other study quite far from the jet for two main reasons. First, the jet being rectangular, the structured grid in the jet region is rectangular and a rectangular

| | $St_{low}$ | $dB_{low}$ | $St_{screech}$ | $dB_{screech}$ | $St_{screech}$ exp. | $St_{Tam}$ |
|---|---|---|---|---|---|---|
| JetTR1 | 0.21 | 135 | 0.36 | 150 | 0.37 | 0.41 |
| JetTR2 | 0.18 | 140 | 0.31 | 159 | 0.31 | 0.33 |
| JetTR25 | 0.17 | 139 | 0.30 | 171 | – | 0.30 |
| JetTR3 | 0.16 | 142 | 0.29 | 174 | 0.28 | 0.28 |

**Table 3. Frequencies $St_{low}$ and $St_{screech}$ and amplitudes $dB_{low}$ and $dB_{screech}$ of the two tone frequencies emerging in Figure 13 for each jet; screech frequency $St_{screech}$exp. found in the experimental study[15]; screech frequency $St_{Tam}$ found using the model of Tam[35].**

FW-H surface is not ideal. Second, it was too expensive in terms of storage to use the method with several outflow disks of Shur et al.[39], used for example by Brès et al.[40] and in the case of an open surface, a "loose" FW-H surface is then preferable[39]. Indeed, this surface located quite far from the jet permits to avoid the creation of "pseudo-sound"[41]. This unphysical sound results from the convection through the surface of slow turbulent structures that are not canceled because of the absence of the outflow disk.

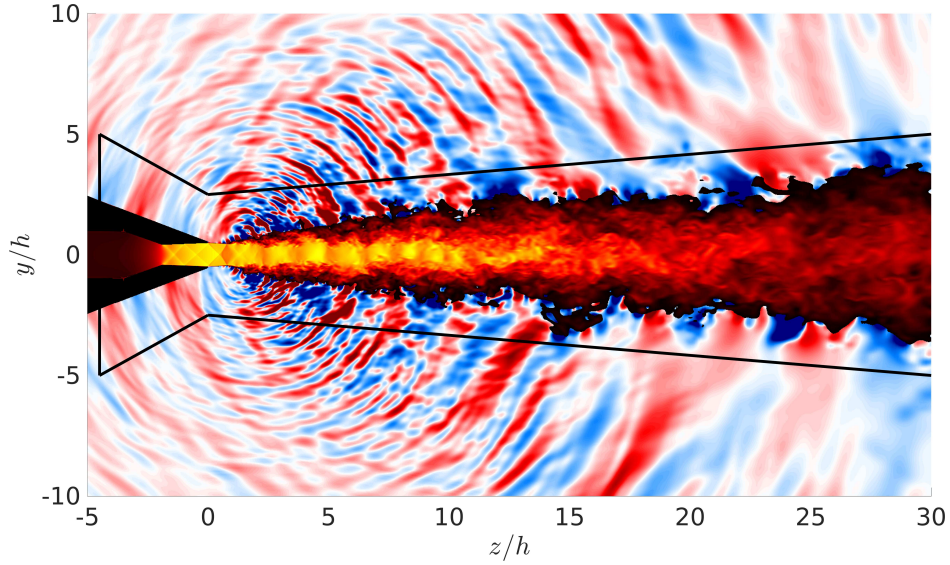


**Figure 14. Representation of the contour of the FW-H surface in black over a 2-D snapshot along the minor axis representing the Mach number in the jet and of the fluctuating pressure around for JetTR2. The nozzle is in black.**

The FW-H surface is used to compute the fluctuating pressure in the far-field at a distance of $40D_{eq}$ along the minor axis. The OASPL directivities as predicted in the far-field of the jet in the minor-axis plane are represented for the four jets in Figure 15 and compared to the experimental results for JetTR1, JetTR2 and JetTR3. Overall, a good agreement is reached.

The acoustic spectra in the far-field are represented in Figure 16 as functions of the Strouhal number and the directivity angle, with 20 degrees being the most upstream location and 160 degrees angle corresponding to the most downstream side angle. Several acoustic components typical of non-ideally expanded supersonic jets can be seen in Figure 16. In the upstream direction, for $\theta < 60$ degrees, the screech tone frequencies dominate, as already pointed out in the pressure spectra of Figure 13. In the downstream direction, $\theta > 140$ degrees, the mixing noise generated by large scale turbulent structures appears around a Strouhal number of 0.25. The direction and frequency of this acoustic component are in good agreement with the numerical results of Berland *et al.*[4] for a planar supersonic jet with $\mathcal{M}_j = 1.55$. A third acoustic component is visible for $60 < \theta < 160$ degrees. Its central frequency is varying with the angle of observation. This component is associated with broadband shock-associated noise, as observed in experimental[9–11] and numerical[4,29] studies. A mechanism was proposed by Harper-Bourne and Fisher[12] for this acoustic component. In this mechanism, the broadband shock-associated noise is generated by the interactions between the turbulent structures propagating downstream in the jet shear layers and the shocks of the shock cell structure. Each interaction is considered as an acoustic source. The directivity of constructive interference is then determined. This model yields a central frequency

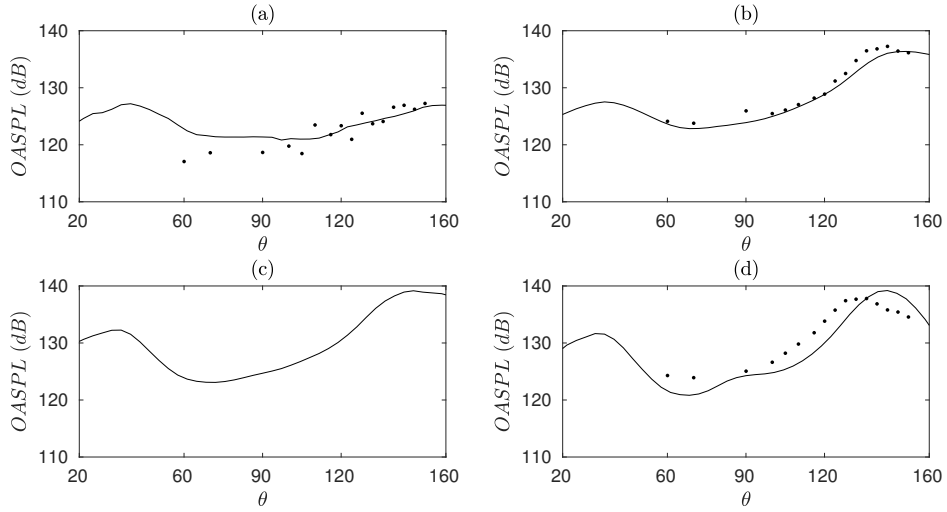


**Figure 15. OASPL obtained on the circle of radius $R = 40D_{eq}$ in the minor axis plane as functions of the angle $\theta$ with respect to the upstream direction for (a) JetTR1, (b) JetTR2, (c) JetTR25 and (d) JetTR3; • experimental results and —— current results (LES & FW-H).**

$$f_{shock} = \frac{N u_c}{L_s(1 + \mathcal{M}_c cos(\theta))} \tag{12}$$

where $N$ is the mode number, $L_s$ is a length scale related to the shock cell size, and $\mathcal{M}_c$ is the convective Mach number. As the cell length varies with the axial direction, it is difficult to chose a value of $L_s$. A value of $L_s = 0.8L_{model}$ is used for our study. The corresponding central frequency of the broadband shock-associated noise is represented with dashed line in Figure 16 for $N = 1$ and using the values in Table 2 for $u_c$ and $\mathcal{M}_c$. A good overall agreement is found. It is worth noting that at angles around $\theta = 80$ degrees, for JetTR2, JetTR25 and JetTR3, the first harmonics of the screech component coincide with the BBSAN component and becomes dominant. The same observation has been made in the experimental study[15]. One can finally note that in the upstream direction, the relation (12) tends to the values of $St = 0.50$, $St = 0.48$, $St = 0.45$ and $St = 0.44$ for JetTR1, JetTR2, JetTR25 and JetTR3, respectively. Those tones are visible in the spectra of figure 13, between the screech tones and their harmonics. Finally, for JetTR2, JetTR25 and JetTR3, a fourth acoustic component is visible at an angle of $\theta = 140$ degrees. This broadband component corresponds to the Mach wave radiation. Its directivity is given by the model of Oertel[13], which writes

$$\theta = 180 - \arccos\left(\frac{1}{\mathcal{M}_c}\right) \tag{13}$$

where $\phi$ is the angle with respect with the jet axis and $\mathcal{M}_c$ is the convective Mach number.

Using a convective Mach number of $\mathcal{M}_c = 1.25$, relation (13) gives an angle of $\theta = 143$ degrees. Please note that this angle is also in agreement with the peak values visible in Figure 15(b-d) for JetTR2, JetTR25 and JetTR3.

## VI. Conclusions

An artificial dissipation mechanism derived from the one of Ducros *et al.*[20] is proposed in the first part of this paper. This mechanism is assessed using linear and non-linear 2-D test cases. The results are presented and demonstrate the ability of the modified solver to perform large-eddy simulations of highly compressible flows. The solver is then used to simulate rectangular supersonic overexpanded jets. The geometry of the nozzle and the exit conditions are similar to those in the experimental study carried out at the University of Cincinnati. A convergence study is first performed. Mean fields are found to be in good agreement with experimental results. Four simulations with different temperature ratios are then presented in order to characterize the effect of the temperature on the aerodynamic and aeroacoustic fields of the jets. First, it is shown that the total number of cells in the shock cell structure decreases with the increase of the temperature ratio. However, the temperature ratio does not influence the size of the first shock cell and

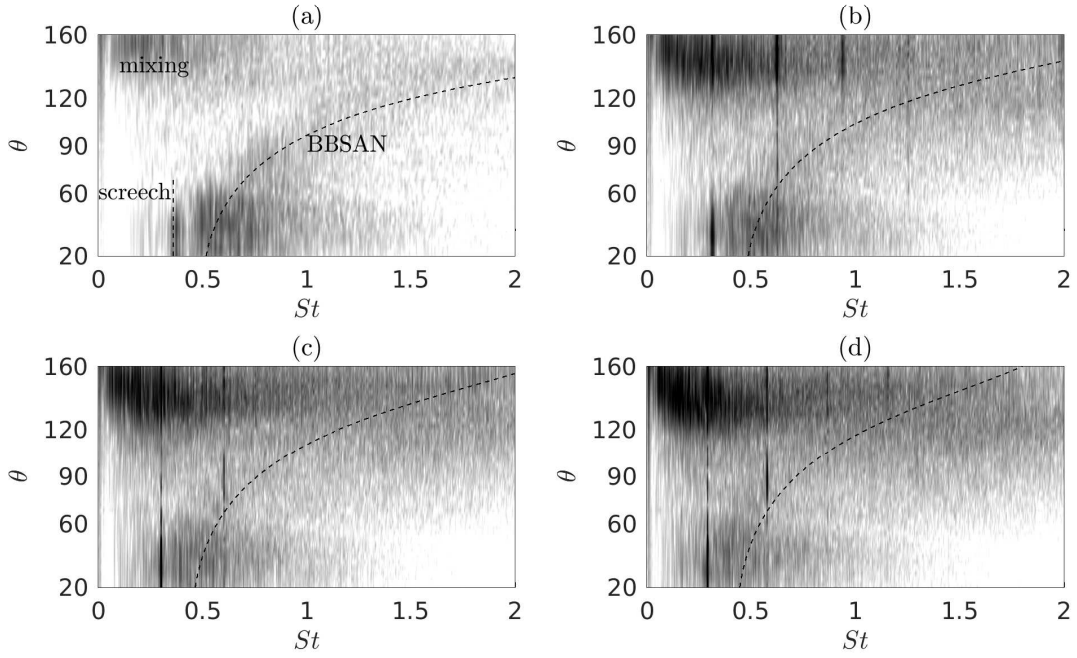


**Figure 16. Far-field SPL as predicted based on the FW-H approach $R = 40D_{eq}$ as functions of the Strouhal number and of the angle $\theta$ with respect to the upstream direction; data in the minor-axis plane of the jet for (a) JetTR1, (b) JetTR2, (c) JetTR25 and (d) JetTR3. The color scale ranges from 110 and 140 dB/St.**

the linear decrease of the shock cell size in the downstream direction. In case of the shock cell structure, results are found to be similar to those for round non-ideally expanded supersonic jets. The Overall Sound Pressure Levels are then represented along the minor and major axis. It is seen that the intensity of the screech feedback mechanism increases with the Temperature Ratio. For JetTR25 and JetTR3, the strong flapping motion of the jet along the minor axis due to the screech feedback mechanism is believed to lead to an asymmetric organization of the Mach wave radiation. Consequently, the convection velocity of the turbulent structures in the jet shear layers along the minor axis is studied. Once normalized by the jet exit velocity, the convection velocity is shown to decrease with the jet temperature ratio, a similar behavior as observed in round jets. In the last part of the paper, the near- and far-field acoustic fields are studied. In the vicinity of the nozzle, a screech frequency is observed for each jet. This frequency is consistent with both experimental data and a theoretical model. The far-field acoustic fields are finally computed using a Ffowcs Williams-Hawkings based approach. Four acoustic components typical of non-ideally supersonic jets are observed, namely the screech noise, the broadband shock-associated noise, the mixing noise and the Mach wave noise. Their directivities and frequencies are in agreement with experimental results and models.

## Acknowledgments

The computations were performed using HPC resources provided by the Swedish National Infrastructure for Computing (SNIC) at the PDC center. Jing Gong at PDC is acknowledged for assistance concerning technical and implementational aspects.

## References


[1] A. Powell. On the mechanism of choked jet noise. *Proceedings of the Physical Society. Section B*, 66(12): 1039–1056, 1953.

[2] G. Raman. Supersonic jet screech: half-century from powell to the present. *J. Sound Vib.*, 225(3): 543–571, 1999.

[3] C. Bogey and C. Bailly. Investigation of downstream and sideline subsonic jet noise using large eddy simulation. *Theor. Comput. Fluid Dyn.*, 20(1):23–40, 2006.

[4] J. Berland, C. Bogey, and C. Bailly. Numerical study of screech generation in a planar supersonic jet. *Phys. Fluids*, 19(7):075105, 2007.

[5] C. Bogey and C. Bailly. An analysis of the correlations between the turbulent flow and the sound pressure fields of subsonic jets. *J. Fluid Mech.*, 583:71–97, 2007.

[6] N.D. Sandham and A.M. Salgado. Nonlinear interaction model of subsonic jet noise. *Phil. Trans. R. Soc. A*, 366:2745–2760, 2008.

[7] C.K.W. Tam. Mach wave radiation from high-speed jets. *AIAA J.*, 47(10):2440–2448, 2009.

[8] D.L. Martlew. Noise associated with shock waves in supersonic jets. aircraft engine noise and sonic boom. *AGARD C.P.*, pages 1–70, 1969.

[9] C.K.W. Tam and H.K. Tanna. Shock associated noise of supersonic jets from convergent-divergent nozzles. *J. Sound Vib.*, 81(3):337–358, 1982.

[10] B. André. *Etude expérimentale de l'effet du vol sur le bruit de choc de jets supersoniques sous-détendus*. PhD thesis, Ecole Centrale de Lyon, 2012. 2012–42.

[11] C.K.W. Tam, J.M. Seiner, and J.C. Yu. Proposed relationship between broadband shock associated noise and screech tones. *J. Sound Vib.*, 110(2):309–321, 1986.

[12] M. Harper-Bourne and M.J. Fisher. The noise from shock waves in supersonic jets. *AGARD C.P.*, 1974.

[13] H. Oertel Sen. *Kinematics of Mach waves inside and outside supersonic jets*. Springer, Berlin, 1979.

[14] E. Gutmark, K.C. Schadow, and C.J. Bicker. Near acoustic field and shock structure of rectangular supersonic jets. *AIAA J.*, 28(7):1163–1170, 1990.

[15] P. Mora, F. Baier, E.J. Gutmark, and K. Kailasanath. Acoustics from a rectangular c-d nozzle exhausting over a flat surface. *AIAA Paper 2016-1884*, 2016.

[16] P. Eliasson. *EDGE: A Navier-Stokes solver for unstructured grids*. 2001.

[17] B. Semlitsch, M. Mihaescu, L. Fuchs, and E. Gutmark. Analyzing the impact of the inlet temperature on the acoustic noise production form a supersonic jet using large eddy simulations. In *Proc. Mtgs. Acoust.*, volume 19, 2013.

[18] B. Semlitsch, M. Mihaescu, and L. Fuchs. Large eddy simulation of fluidic injection into a supersonic convergent-divergent duct. In *Direct and Large-Eddy Simulation IX*, pages 297–302. 2015.

[19] A. Jameson, W. Schmidt, and E. Turkel. Numerical solutions of the euler equations by finite volume methods using runge-kutta time-stepping schemes. *AIAA paper 1981-1259*, 1981.

[20] F. Ducros, V. Ferrand, F. Nicoud, C. Weber, D. Darracq, C. Gacherieu, and T. Poinsot. Large-eddy simulation of the shock/turbulence interaction. *J. Comput. Phys.*, 152(2):517–549, 1999.

[21] J.C. Hardin, J. Ristorcelli, and C.K.W. Tam. Icase/larc workshop on benchmark problems in computational aeroacoustics (caa). 1995.

[22] C.K.W. Tam and J.C. Webb. Dispersion-relation-preserving finite difference schemes for computational acoustics. *J. Comput. Phys.*, 107(2):262–281, 1993.

[23] C. Bogey and C. Bailly. Three-dimensional non-reflective boundary conditions for acoustic simulations : far field formulation and validation test cases. *Acta Acust. United Ac.*, 88:463–471, 2002.

[24] C. Bogey, N. de Cacqueray, and C. Bailly. A shock-capturing methodology based on adaptative spatial filtering for high-order non-linear computations. *J. Comput. Phys.*, 228(5):1447–1465, 2009.

[25] O. Inoue. Propagation of sound generated by weak shock–vortex interaction. *Phys. Fluids*, 12(5):1258–1261, 2000.

[26] R. Westley and J.H. Woolley. The near field sound pressures of a choked jet during a screech cycle. *AGARD C.P.*, 42:23.1–23.13, 1969.

[27] J. Panda, G. Raman, and K.B.M.Q. Zaman. Underexpanded screeching jets from circular, rectangular and elliptic nozzles. *AIAA Paper 97-1623*, 1997.

[28] B. André, T. Castelain, and C. Bailly. Investigation of the mixing layer of underexpanded supersonic jets by particle image velocimetry. *IJHFF*, 50:188–200, 2014.

[29] M.D. Dahl. Predictions of supersonic jet mixing and shock-associated noise compared with measured far-field data. *NASA Technical Report*, TM-2010-216328, 2010.

[30] J. Panda and R.G. Seasholtz. Experimental investigation of density fluctuations in high-speed jets and correlation with generated noise. *J. Fluid Mech.*, 450:97–130, 2002.

[31] J.W. Nichols and S.K. Lele. Large eddy simulation of crackle noise in hot supersonic jets. *J. Acoust. Soc. Am.*, 134(5):4128–4138, 2013.

[32] Y. Hsia, A. Krothapalli, D. Baganoff, and K/ Karamcheti. Effects of mach number on the development of a subsonic rectangular jet. *AIAA J.*, 21(2):176–177, 1983.

[33] K.B.M.Q. Zaman. Spreading characteristics of compressible jets from nozzles of various geometries. *J. Fluid Mech.*, 383:197–228, 1999.

[34] C.K.W. Tam, J.A. Jackson, and J.M. Seiner. A multiple-scales model of the shock-cell structure of imperfectly expanded supersonic jets. *J. Fluid Mech.*, 153:123–149, 1985.

[35] C.K.W. Tam. The shock-cell structures and screech tone frequencies of rectangular and non-axisymmetric supersonic jets. *J. Sound Vib.*, 121(1):135–147, 1988.

[36] R. Gojon, C. Bogey, and O. Marsden. Investigation of tone generation in ideally expanded supersonic planar impinging jets using large-eddy simulation. *J. Fluid Mech.*, 808:90–115, 2016.

[37] R. Gojon, C. Bogey, and O. Marsden. Large-eddy simulation of underexpanded round jets impinging on a flat plate 4 to 9 radii downstream from the nozzle. *AIAA Paper 2015-2210*, 2015.

[38] J. Liu, A. Corrigan, K. Kailasanath, and E. Gutmark. Effects of temperature on noise generation in supersonic jets. *AIAA paper 2016-2937*, 2016.

[39] M.L. Shur, P.R. Spalart, and M.K. Strelets. Noise prediction for increasingly complex jets. part i: Methods and tests. *Int. J. Aeroacoust.*, 4(3):213–245, 2005.

[40] G.A. Brès, F.E. Ham, J.W. Nichols, and S.K. Lele. Nozzle wall modeling in unstructured large eddy simulations for hot supersonic jet predictions. *AIAA paper 2013-2142*, 2013.

[41] D.G. Crighton, A.P. Dowling, J.E. Ffowcs Williams, M.A. Heckl, and F.A. Leppington. *Ffowcs Williams, J.E., Noise Source Mechanisms, in: Modern Methods in Analytical Acoustics: Lecture Notes.* 1992.